

Effects of Nb and Mo additions on thermal behavior, microstructure and magnetic property of FeCoZrBGe alloy

Yaming Sun(孙亚明), Zhiqun Wang(王志群), Shi-Chong Xu(徐仕翀), and Zhong Hua(华中)
Citation: Chin. Phys. B, 2021, 30 (**3**): 038103. DOI: 10.1088/1674-1056/abc7a8
Journal homepage: http://cpb.iphy.ac.cn; http://iopscience.iop.org/cpb

What follows is a list of articles you may be interested in

High temperature strain glass in Ti-Au and Ti-Pt based shape memory alloys

Shuai Ren(任帅), Chang Liu(刘畅), and Wei-Hua Wang(汪卫华)
Chin. Phys. B, 2021, 30 (**1**): 018101. DOI: 10.1088/1674-1056/abc54a

Modeling of microporosity formation and hydrogen concentration evolution during solidification of an Al-Si alloy

Qingyu Zhang(张庆宇), Dongke Sun(孙东科), Shunhu Zhang(章顺虎), Hui Wang(王辉), Mingfang Zhu(朱鸣芳)
Chin. Phys. B, 2020, 29 (**7**): 078104. DOI: 10.1088/1674-1056/ab8abb

Dependence of mechanical properties on the site occupancy of ternary alloying elements in γ'-Ni_3Al: *Ab initio* description for shear and tensile deformation

Minru Wen(文敏儒), Xing Xie(谢兴), Huafeng Dong(董华锋), Fugen Wu(吴福根), Chong-Yu Wang(王崇愚)
Chin. Phys. B, 2020, 29 (**7**): 078103. DOI: 10.1088/1674-1056/ab8a38

Mg acceptor activation mechanism and hole transport characteristics in highly Mg-doped AlGaN alloys

Qing-Jun Xu(徐庆君), Shi-Ying Zhang(张士英), Bin Liu(刘斌), Zhen-Hua Li(李振华), Tao Tao(陶涛), Zi-Li Xie(谢自力), Xiang-Qian Xiu(修向前), Dun-Jun Chen(陈敦军), Peng Chen(陈鹏), Ping Han(韩平), Ke Wang(王科), Rong Zhang(张荣), You-Liao Zheng(郑有炓)
Chin. Phys. B, 2020, 29 (**5**): 058103. DOI: 10.1088/1674-1056/ab7e93

Atomically flat surface preparation for surface-sensitive technologies

Cen-Yao Tang(唐岑瑶), Zhi-Cheng Rao(饶志成), Qian-Qian Yuan(袁茜茜), Shang-Jie Tian(田尚杰), Hang Li(李航), Yao-Bo Huang(黄耀波), He-Chang Lei(雷和畅), Shao-Chun Li(李绍春), Tian Qian(钱天), Yu-Jie Sun(孙煜杰), Hong Ding(丁洪)
Chin. Phys. B, 2020, 29 (**2**): 028101. DOI: 10.1088/1674-1056/ab6586

Effects of Nb and Mo additions on thermal behavior, microstructure and magnetic property of FeCoZrBGe alloy*

Yaming Sun(孙亚明)[1], Zhiqun Wang(王志群)[2], Shi-Chong Xu(徐仕翀)[1], and Zhong Hua(华中)[1,†]

[1] National Demonstration Center for Experimental Physics Education, Jilin Normal University, Siping 136000, China
[2] State Grid Economic Research Institute of East Inner Mongolia Electric Power Company Limited, Hohhot 010020, China

(Received 17 September 2020; revised manuscript received 22 October 2020; accepted manuscript online 5 November 2020)

Both Nb and Mo additions play a vital role in FeCo-based alloys and it is crucial to understand their roles and contents on thermal behavior, microstructural feature and magnetic property of alloys. Nanocrystalline alloy ribbons $Fe_{40}Co_{40}Zr_{9-y}M_yB_{10}Ge_1$ (y = 0–4; M = Nb, Mo) were prepared by crystallizing the as-quenched amorphous alloys. The effects of Nb and Mo additions on structures and properties of the $Fe_{40}Co_{40}Zr_9B_{10}Ge_1$ alloy are investigated systemically and compared. With increasing Nb or Mo content, the primary crystallization temperature, grain size of α-Fe(Co) phase and coercivity H_c all decrease. Moreover, the effect of Mo addition on thermal behavior, microstructure and magnetic properties of the FeCoZrBGe alloy is greater compared to Nb addition. The gap between primary and secondary crystallization peaks of Mo-containing alloys is wider than that of Nb-containing alloys. Both grain size and H_c of Mo-containing alloys are smaller than those of Nb-containing alloys. For $Fe_{40}Co_{40}Zr_9B_{10}Ge_1$ alloy, high Mo addition proportion is better compared to high Nb addition proportion.

Keywords: alloy, Nb addition, Mo addition, transmission electron microscopy

PACS: 81.07.Bc, 75.75.–c **DOI:** 10.1088/1674-1056/abc7a8

1. Introduction

Fe-based nanocrystalline materials as one kind of the fundamental functional materials of electronic industry promote the development of related industries to the direction of high efficiency, energy saving and green environmental protection, playing a great role in promoting the progress of modern power and electrical industry technology, which has drawn a great deal of attention.[1–6]

Doping engineering is an effective method and widely used to tailor structures and properties of nanoscale materials, facilitating the construction of various multifunctional materials and devices. It has been reported that transition metals doped in Fe-based alloys have important effects.[7–9] Nb and Mo are popular adding elements due to the fact that they can improve microstructure and properties of Fe-based alloys effectively.[10,11] Moreover, the effects of Nb and Mo on microstructure and properties of Fe-based alloys have some difference. For FeCuVSiB alloys, Mo was not as effective as Nb in limiting grain growth.[12] For Mo-doped $Fe_{73.5}Si_{13.5}B_9Nb_{3-x}Mo_xCu_1$ (x = 0, 1.5, 2 and 3) alloys, when Nb was gradually replaced by Mo, the thermal stabilities of both the ferro-paramagnetic transition of the amorphous phase and the precipitation of the α''-$Fe_{1-x}Si_x$ phase were found to deteriorate.[13] For Fe–Si–B–M–Cu (M = Nb, Mo) alloys, replacing Nb by Mo can enhance oxidation resistance.[14]

Our research team has been engaged in the research of FeCoZrB alloys for a long time.[15–17] There is a large heat of mixing between the members of this series. During the process of crystallization, besides Fe(Co) crystallization phase, metastable phase or $ZrCo_3B_2$ phase can easily form. Adding Nb can slightly reduce the negative enthalpy of mixing of this alloy system, while adding Mo will significantly reduce the negative enthalpy of mixing of this alloy system.[18] Theoretically, the effect of Mo addition on the crystallization phase should be greater than that of Nb addition, which is different from other alloys.[11–14] In this paper, $Fe_{40}Co_{40}Zr_{9-y}M_yB_{10}Ge_1$ (y = 0–4; M = Nb, Mo) amorphous alloys were prepared and annealed at their primary crystallization peak. The effects of Nb and Mo contents on the microstructure and properties of FeCoZrBGe alloys are investigated systemically and compared, to explore which element is more beneficial to microstructure and properties for the $Fe_{40}Co_{40}Zr_9B_{10}Ge_1$ alloy.

2. Experimental details

Nominal composition $Fe_{40}Co_{40}Zr_{9-y}M_yB_{10}Ge_1$ (y = 0, 1, 2, 3, 4; M = Nb, Mo) alloy ingots were prepared by arc melting with the mixtures of high pure elements. The ingots were remelted for 4 times with the magnetic stirring to ensure the homogeneity under the protection of high purity argon. Then mother alloy ingots were put into a special quartz tube. Amorphous alloy ribbons of $Fe_{40}Co_{40}Zr_{9-y}M_yB_{10}Ge_1$ (y = 0, 1, 2, 3, 4; M = Nb, Mo) were prepared by a single roller melt spinning technique (the copper-wheel rate is 38 m/s) and

*Project supported by the National Natural Science Foundation of China (Grant No. 51301075) and supported by Sinoma Institute of Materials Research (Guang Zhou) Co., Ltd.

†Corresponding author. E-mail: huazhong196110@163.com

© 2021 Chinese Physical Society and IOP Publishing Ltd

annealed at their primary crystallization peak in vacuum.

Differential scanning calorimetry (DSC) was recorded by a simultaneous thermal analyzer (STA, 449F5). The structures of alloys were checked by x-ray diffractometer (XRD, D/max 2500/PC, Cu-$K\alpha$, $\lambda = 1.5406$ Å, 40 kV, 200 mA). Grain size D of α-Fe(Co) crystals was calculated by Jade 5.0. Microstructures were analyzed by transmission electron microscopy (TEM, FEI Talos F200). Fischione Model 1050 TEM Mill was used to prepare TEM samples. Using digitalmicrograph software to analyze TEM images. Coercivity H_c was measured by a DC B–H loop tracer (RIKEN BHS40).

3. Results and discussion

Figure 1 shows the DSC traces of $Fe_{40}Co_{40}Zr_{9-y}M_yB_{10}Ge_1$ ($y = 0$, 1, 2, 3, 4; M = Nb, Mo) amorphous alloys. Both the shape and the location of crystallization peaks change with the addition of Nb and Mo. There are three exothermic peaks in the DSC trace of the $Fe_{40}Co_{40}Zr_9B_{10}Ge_1$ alloy. With the increase of Nb/Mo content, the primary crystallization temperature T_{p1} shifts to low temperature. The deviation of the secondary crystallization peak, T_{p2}, is irregular and the third crystallization temperature T_{p3} shifts to high temperature. The shift of primary crystallization temperature T_{p1} is related to the atomic radii. The atomic radii of Zr, Nb and Mo is 0.160, 0.148 and 0.140 nm, respectively. During the crystallization process, Zr, Nb and Mo distribute in the residual amorphous matrix. The diffusion rate of atomic with small radius is fast, which decreases the crystallization temperature of the system. Therefore, the primary crystallization temperature T_{p1} shifts to low temperature with the increase of Nb or Mo content.

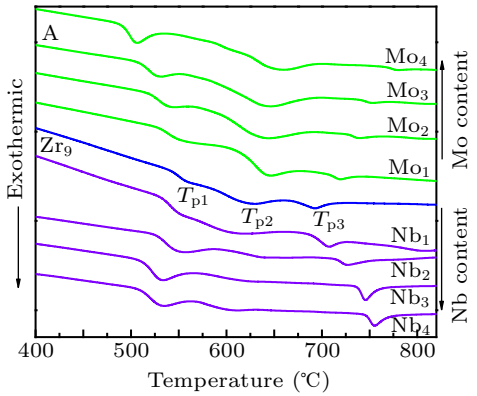


Fig. 1. DSC traces of as-quenched $Fe_{40}Co_{40}Zr_{9-y}M_yB_{10}Ge_1$ ($y = 0$, 1, 2, 3, 4; M = Nb, Mo) alloys.

The primary crystallization peak (T_{p1}) and the secondary crystallization peak (T_{p2}) of $Fe_{40}Co_{40}Zr_{9-y}M_yB_{10}Ge_1$ ($y = 0$, 1, 2, 3, 4; M = Nb, Mo) alloys are shown in Fig. 2. The gap between the primary crystallization (T_{p1}) and the secondary crystallization peak (T_{p2}) of the Mo-containing alloys is much wider compared to the Nb-containing alloys. In addition, the higher the content of Mo is, the wider the gap is. When addition ratio is 4 at%, the effect of Nb is far less than that of Mo on the gap between primary and secondary crystallization temperatures. Adding Mo can increase the annealing scope effectively and the temperature interval can reach 150.5 K when Mo addition is 4 at%.

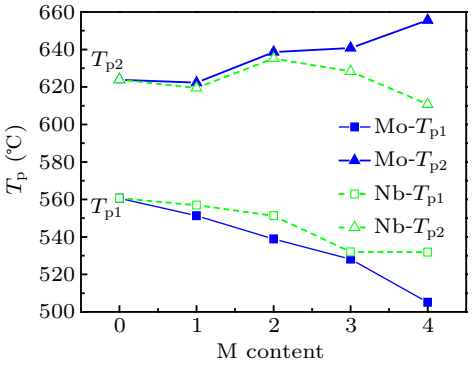


Fig. 2. Primary crystallization peak (T_{p1}) and secondary crystallization peak (T_{p2}) of $Fe_{40}Co_{40}Zr_{9-y}M_yB_{10}Ge_1$ ($y = 0$, 1, 2, 3, 4; M = Nb, Mo) alloys.

XRD of $Fe_{40}Co_{40}Zr_{9-y}M_yB_{10}Ge_1$ ($y = 0$, 1, 2, 3, 4; M = Nb, Mo) amorphous alloys annealed at crystallization peak temperatures is given in Fig. 3. For the $Fe_{40}Co_{40}Zr_9B_{10}Ge_1$ alloy, α-Fe(Co) phase, β-Mn type phase and amorphous phase are observed. The crystallization volume fraction is low. For the Mo-containing and Nb-containing alloys, the primary crystallization phase is only α-Fe(Co) phase. There is almost no shift of diffraction peak. With the increase of Mo and Nb content, the diffraction peak strength of α-Fe(Co) phase increases. In other words, the crystallization volume fraction of α-Fe(Co) phase increases with the increase of Mo and Nb content.

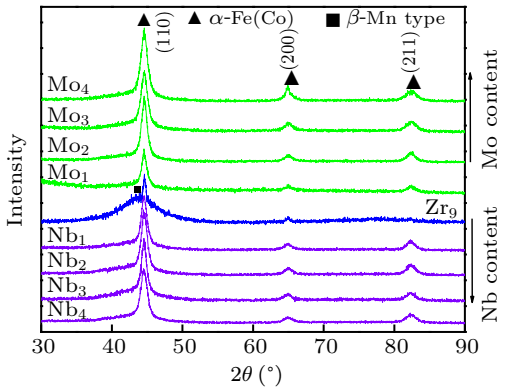


Fig. 3. XRD of $Fe_{40}Co_{40}Zr_{9-y}M_yB_{10}Ge_1$ ($y = 0$, 1, 2, 3, 4; M = Nb, Mo) amorphous alloys after annealing.

According to the results of XRD, the grain sizes [α-Fe(Co)] of $Fe_{40}Co_{40}Zr_{9-y}M_yB_{10}Ge_1$ ($y = 1$, 2, 3, 4; M = Nb, Mo) alloys after annealing are given in Fig. 4. With the increase of Nb and Mo content, the grain size decreases. The downward trends are obvious. At the same content of Mo and Nb, the grain size [α-Fe(Co)] of Mo-containing alloys is lower compared to Nb-containing.

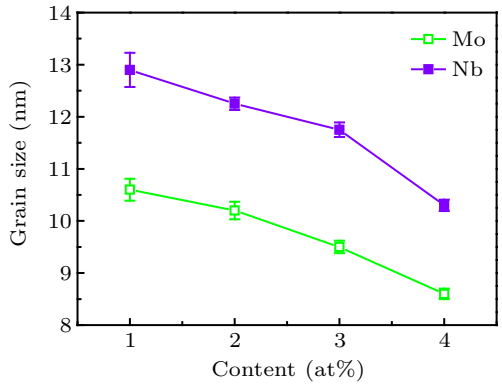


Fig. 4. Grain sizes [α-Fe(Co)] of $Fe_{40}Co_{40}Zr_{9-y}M_yB_{10}Ge_1$ (y = 1, 2, 3, 4; M = Nb, Mo) alloys with different M contents.

Figure 5 gives the transmission electron microscopy (TEM) images, the corresponding selected-area electron diffraction (SAED) patterns, high resolution transmission electron microscope (HRTEM) images, fourier transform (FFT) images and grain-size distribution images of $Fe_{40}Co_{40}Zr_{9-y}M_yB_{10}Ge_1$ (y = 0, 4; M = Nb, Mo) alloys after annealing. The TEM image and SAED pattern of $Fe_{40}Co_{40}Zr_9B_{10}Ge_1$ alloy are shown in Fig. 5(a1). The diffraction rings of α-Fe(Co) phase and β-Mn type phase are indexed. The enlarged area of A and B are shown in Figs. 5(a2) and 5(a3), respectively. The corresponding fast fourier transform (FFT) images are shown in the upper right corner. For Fig. 5(a2), the FFT shows that the zone axis is body-centered cubic [111] and grain A is α-Fe(Co). For Fig. 5(a3), the FFT shows that the zone axis is cubic [411] and grain B is β-Mn type. The TEM image and SAED pattern of the $Fe_{40}Co_{40}Zr_5Nb_4B_{10}Ge_1$ alloy are shown in Fig. 5(b1), and the diffraction rings of α-Fe(Co) phase are indexed. The enlarged area is shown in Fig. 5(b2). The calculated d-space is 0.201 nm, which is consistent with the value for (110) plane of α-Fe(Co) phase. From Fig. 5(b3), the mean grain size is approximately 8.9 nm. The TEM image and SAED pattern of the $Fe_{40}Co_{40}Zr_5Mo_4B_{10}Ge_1$ alloy are shown in Fig. 5(c1),

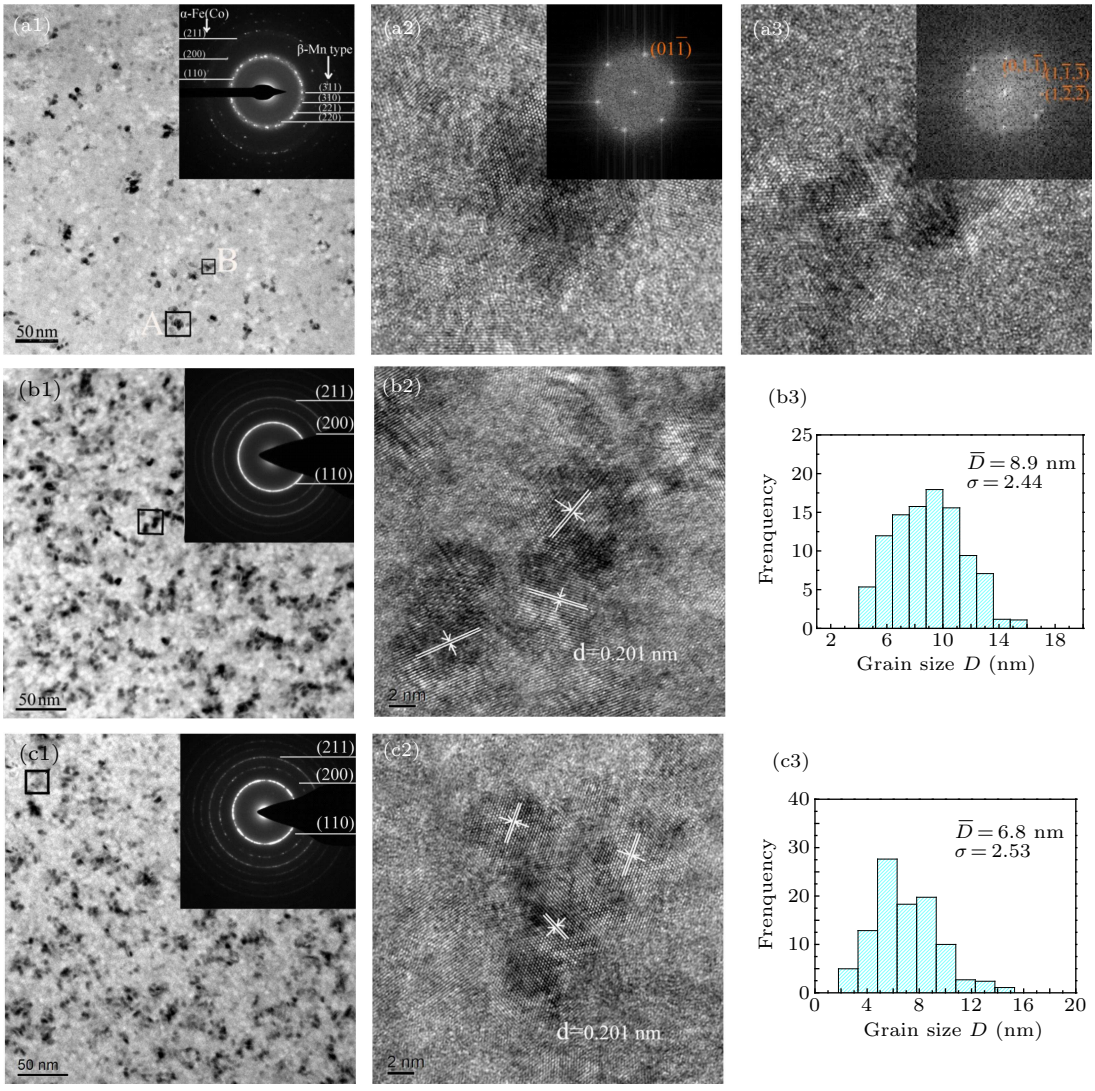


Fig. 5. Transmission electron microscopy (TEM) images [(a1), (b1), (c1)], the corresponding selected-area electron diffraction (SAED) patterns [the upper right corner of [(a1), (b1), (c1)], high resolution transmission electron microscope images [(a2), (a3), (b2), (c2)], Fourier transform (FFT) images [the upper right corner of (a2), (a3)] and grain-size distribution images [(b3), (c3), (c3)] of alloys after annealing. (a) $Fe_{40}Co_{40}Zr_9B_{10}Ge_1$, (b) $Fe_{40}Co_{40}Zr_5Nb_4B_{10}Ge_1$, (c) $Fe_{40}Co_{40}Zr_5Mo_4B_{10}Ge_1$.

Table 1. Enthalpy of mixing between Zr/Nb/Mo and other elements.

	Enthalpy of mixing (kJ/mol)				
	Fe	Co	Zr	B	Ge
Zr	−25	−41		−71	−72.5
Nb	−16	−25	+4	−54	−36.5
Mo	−2	−5	−6	−34	−13.5

and the diffraction rings of α-Fe(Co) phase are indexed. The fine α-Fe(Co) nanocrystals are found to be distributed in the residual amorphous phase. An enlarged area is shown in Fig. 5(c2). The calculated d-space is 0.201 nm, which is consistent with the value for (110) plane of α-Fe(Co) phase. From Fig. 5(b3), the mean grain size is approximately 6.8 nm. From the TEM images [Figs. 5(a1), 5(b1), 5(c1)], both the crystallization volumes fraction of $Fe_{40}Co_{40}Zr_5Nb_4B_{10}Ge_1$ alloy and $Fe_{40}Co_{40}Zr_5Mo_4B_{10}Ge_1$ alloy are larger than that of the $Fe_{40}Co_{40}Zr_9B_{10}Ge_1$ alloy without additive elements. From the HRTEM images [Figs. 5(a2), 5(b2), 5(c2)], the grain size [α-Fe(Co)] of the $Fe_{40}Co_{40}Zr_9B_{10}Ge_1$ alloy is larger than that of the Nb- and Mo-containing alloys. The width of grain-size distribution can be determined by the geometric standard deviation (σ). From grain-size distribution [Figs. 5(b3) and 5(c3)], the geometric standard deviation (σ) for the grain size distribution of Mo-containing alloy with 4 at% Mo is sightly broader than that of Nb-containing alloy with 4 at% Nb.

Our research team has been engaged in the research of FeCoZrB alloys for a long time. During the process of crystallization, besides α-Fe(Co) crystallization phase, metastable phase or $ZrCo_3B_2$ phase can easily form.[15–17] Table 1 gives the enthalpy of mixing between Zr/Nb/Mo and other elements.[18] There is a large negative enthalpy of mixing between the elements of FeCoZrBGe. Compared with Zr, adding Nb reduces the negative enthalpy of mixing, but adding Mo significantly reduces the enthalpy of mixing. If there is a large negative enthalpy of mixing among members, there is a greater attraction among members. The additions of Nb and Mo reduce the negative enthalpy of mixing, thus reducing the attraction between members and resulting in the difference of crystallization products. The effect of Mo addition on the crystallization phase of FeCoZrBGe alloys is greater than that of Nb addition.

H_c of $Fe_{40}Co_{40}Zr_{9-y}M_yB_{10}Ge_1$ ($y = 0$, 1, 2, 3, 4; M = Nb, Mo) alloys with different M contents is shown in Fig. 6. The large H_c of $Fe_{40}Co_{40}Zr_9B_{10}Ge_1$ alloy is due to the precipitation of β-Mn type phase. With increasing the M content, H_c decreases and the decrease of H_c for Mo-containing alloys is more obvious. For the Nb-containing and Mo-containing alloys, only α-Fe(Co) phase precipitates from amorphous matrix. H_c of Mo-containing alloy is lower compared to the Nb-containing alloy. Suzuki *et al.*[19] revealed that the value of H_c is in direct proportion to D^6 and V_{cry}. From Figs. 4 and 5, it is clear that the grain size of Nb-containing alloys is larger than that of Mo-containing alloys under the same proportion. The downward trends of grain size are obvious, which could result in the decrease of H_c quickly. However, the crystallization volume fraction of α-Fe(Co) phase increases with the increase of Mo and Nb contents, which could result in the increase of H_c. Bitoh *et al.*[20] revealed that the value of H_c is also related to the width of grain-size distribution of α-Fe nanocrystals and H_c increases with increasing width of the grain-size distribution. The width of grain-size distribution of Mo-containing alloy with 4 at% Mo is slightly broader than that of Nb-containing alloy with 4 at% Nb [Figs. 5(b3) and 5(c3)]. Therefore, the downward trends of H_c become slow with the increase of Mo and Nb content.

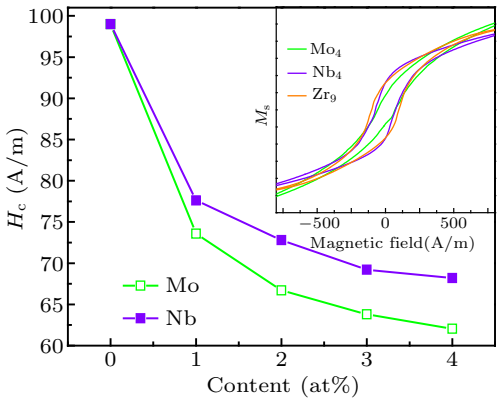


Fig. 6. Coercivity (H_c) of $Fe_{40}Co_{40}Zr_{9-y}M_yB_{10}Ge_1$ ($y = 0$, 1, 2, 3, 4; M = Nb, Mo) alloys with different M contents.

4. Conclusion

Amorphous alloy ribbons of $Fe_{40}Co_{40}Zr_{9-y}M_yB_{10}Ge_1$ ($y = 0$, 1, 2, 3, 4; M = Nb, Mo) prepared by melt spinning were annealed at their crystallization peak temperatures. The effect of M content on thermal behavior, microstructure and magnetic property were investigated systemically and compared. The effect of Mo addition is greater compared to Nb addition.

(1) With increasing Nb or Mo content, the primary crystallization temperature decreases. The gap between primary and secondary crystallization peaks of Mo-containing alloys is wider compared to Nb-containing alloys.

(2) For the $Fe_{40}Co_{40}Zr_9B_{10}Ge_1$ alloy, the primary crystallization phases of α-Fe(Co) and β-Mn type are observed. For the Mo-containing and Nb-containing alloys, the primary crystallization phase is only α-Fe(Co) phase. With increasing Nb or Mo content, the grain size of α-Fe(Co) phase decreases. The grain size of Mo-containing alloy is smaller compared to Nb-containing alloy under the same proportion.

(3) With increasing Nb or Mo content, H_c decreases. H_c of Mo-containing alloy is smaller compared to Nb-containing alloy under the same proportion. For $Fe_{40}Co_{40}Zr_9B_{10}Ge_1$ alloy, high Mo addition proportion (4 at%) has better effect than high Nb addition proportion on the annealing scope, grain size and H_c.

References

[1] Liu T, Li F C, Wang A D, Xie L, He Q F, Luan J H, He A N, Wang X M, Liu C T and Yang Y 2019 *J. Alloys Compd.* **776** 606

[2] Jha R, Diercks D R and Chakraborti N 2019 *Scripta Mater.* **162** 331

[3] Mchenry M E, Willard M A and Laughlin D E 1999 *Prog. Mater. Sci.* **44** 291

[4] Xie L, Liu T, He A, Li Q, Gao Z K, Wang A D, Chang C T, Wang X M and Liu C T 2018 *J. Mater. Sci.* **53** 1437

[5] Wang Y C, Zhang Y, Kawazoe Y, Shen J and Cao C D 2018 *Chin. Phys. B* **27** 116401

[6] Xie L, Wang A D, Yue S Q, He A N, Chang C T, Li Q, Wang X M and Liu C T 2019 *J. Magn. Magn. Mater.* **483** 158

[7] Lashgari H R, Chu D, Xie S, Sun H, Ferry M and Li S 2014 *J. Non-Cryst. Solids* **319** 61

[8] Zhang L, Wang Z and Xu Y C 2018 *J. Non-Cryst. Solids* **481** 148

[9] Li Y, Wang Z and Zhang W 2018 *AIP Adv.* **8** 056115

[10] Zhang J W, Zhang X Y, Xiao F R, Liu J H and Zheng Y Z 1998 *Mater. Lett.* **36** 223

[11] Perduta K, Zbroszczyk J, Olszewski J, Fukunaga H, Ciurzyńska W, Hasiak M and Lelątko J 2006 *J. Magn. Magn. Mater.* **304** e862

[12] Lu W, Fan J W, Wang Y X and Yan B 2010 *J. Magn. Magn. Mater.* **322** 2935

[13] Silveyra J M, Illeková E, Švec P, Janičkovič D, Rosales-Rivera A and Cremaschi V J 2010 *Physica B* **405** 2720

[14] Silveyra J M and Illekov E 2014 *J. Alloy Compd.* **610** 180

[15] Yu W Q, Zeng H Q, Sun Y M and Hua Z 2017 *Phys. Lett. A* **381** 1573

[16] Yu W Q, Long D, Liu Y D, Sun Y M and Hua Z 2015 *Acta Phys. Pol. A* **128** 340

[17] Yu W Q, Sun Y M and Hua Z 2011 *Appl. Surf. Sci.* **257** 9733

[18] Takeuchi A and Inoue A 2005 *Mater. Trans.* **46** 2817

[19] Suzuki K, Cadogan J M 1998 *Phys. Rev. B* **58** 2730

[20] Bitoh T, Makino A, Inoue A and Masumoto T 2003 *Mater. Trans.* **44** 2011